

# **Birefringence Prediction of Optical Media**

Bingfeng Fan

*Department of Mechanical & Industrial Engineering  
University of Massachusetts Amherst  
Amherst, MA 01003*

David O. Kazmer\*

*Department of Plastics Engineering  
University of Massachusetts Lowell  
Lowell, MA 01854*

Wit C. Bushko

*GE Corporate Research and Development  
Schenectady, NY 12301*

Richard P. Theriault *and* Andrew J. Poslinski

*GE Plastics  
One Plastics Avenue  
Pittsfield, MA 01201*

**REVISED SUBMISSION TO**

**POLYMER ENGINEERING AND SCIENCE**

18-June-2003

---

\* Author to whom correspondence should be addressed: Dept. of Plastics Engineering, Lowell, MA 01854

## ABSTRACT

The flow and thermally induced birefringence of injection-compression molded optical media such as compact discs and digital video discs is predicted by applying a stress-optical rule to the flow and thermally induced stresses, which are estimated with a viscoelastic material model integrated into a non-isothermal compressible flow simulation. The resulting model considers flow and cooling induced molecular orientation, and the transient effect of thermal stress and pressure. Contrary to previous research for polystyrene, the validated results indicate that, for polycarbonate, the magnitude of the thermally induced birefringence is comparable to the flow induced birefringence. Simulation results of the flow and thermally induced in-plane birefringence for compact-disc-recordable moldings with an optical grade of polycarbonate compared well with experimental observations at different mold and melt temperatures. Both simulation and experiments indicate that mold and melt temperatures have a significant effect on the level of birefringence; increasing mold or melt temperature significantly reduces the birefringence.

**Keywords:** birefringence; optical media; polycarbonates; injection-compression; viscoelastic properties; compact disc molding.

## INTRODUCTION

Optical media such as compact discs (CDs) and digital video discs (DVDs) are typically injection-compression molded with an optical grade of polycarbonate (PC). One critical quality of the mass produced optical media is birefringence, which reduces the signal-to-noise ratio in the player by causing optical aberration of the reader spot. For the injection-compression molded parts, there are two types of birefringence (1): flow induced birefringence and thermally induced birefringence. The first type is caused by the shear induced molecular orientation developed during the filling and packing stages, and may be frozen in the solidified layers during the cooling of the polymer melt. The second type is caused by the cooling induced molecular orientation and thermally induced residual stress in the molded parts that results from the rapid cooling process coupled with the viscoelastic properties of the polymer.

The stress-optical rule states that the birefringence is proportional to the applied stress difference:  $\Delta n = C\Delta\sigma$ . This rule was experimentally verified for a variety of polymer melts (2, 3). Researchers have applied the stress-optical rule in numerical simulations of flow birefringence (4-9), wherein most of the studies have considered polystyrene (PS) with a high molecular weight. It has been reported that the stress-optical coefficient (SOC) of PS in the glassy state is much lower than that in the melt state (2, 10), and as a result, the birefringence caused by the thermally induced stresses is negligible compared with the flow induced birefringence. These findings explain the largely good agreement between the flow birefringence prediction alone and the experimentally measured residual birefringence of PS in the afore mentioned references (4-9). However, for optical

grades of PC, the molecules are specially truncated for easy flow and low molecular orientation with low flow induced birefringence. The stress optical sensitivity of the optical grades of PC in the glassy state is observed to be comparable to that in the melt state, and thus the effect of thermally induced birefringence cannot be neglected.

The literature of the residual birefringence of PC has been focused on experimental investigations. Wu and White (11) tried to interpret the mechanisms of birefringence development in injection molding by studying the shapes and orientations of the refractive index ellipsoids in compression and injection molded PC strips. The observed residual birefringence was interpreted as the superposition of the birefringence from quenching during cooling and the birefringence from flow orientation during filling. Wimberger-Friedl et al. (12-16), by observing experimentally the birefringence of quenched and injection molded PC samples, have shown that the molecular orientation induced by the transient thermal stress above  $T_g$  is frozen in during vitrification. The birefringence from cooling induced orientation is comparable in magnitude to that from flow induced orientation. In addition, based on the experimental observations, Wimberger-Fiedl (16) has shown that the transient thermally and pressure induced stresses in the vitrifying layers contribute to the residual birefringence, and causes the maximum at the surface in the gapwise distribution of residual birefringence.

Compared with these previous experimental investigations, numerical simulations of residual birefringence of injection or injection-compression molded PC parts are few, and a numerical simulation that considers all the contributions, i.e., the flow and thermally induced molecular orientation, pressure and thermally induced residual stress, and the transient thermal stress, was not found in the literature. Friedrichs et al. (17) numerically

calculated the thermally induced birefringence of PC discs, wherein the linear stress-optical rule is applied, and the effect of the transient thermal stress is not considered. Wimberger-Friedl et al. (12, 14, 18) reported a numerical program of calculating the birefringence of quenched samples by employing a viscous-elastic material model. Material coefficients including shear modulus and SOC were divided into rubbery and glassy components. Above a certain temperature  $T_r$ , a viscous model was employed with a temperature dependent viscosity. Below  $T_r$ , an elastic model was employed with a rubbery shear modulus between  $T_r$  and  $T_g$ , and a glassy shear modulus below  $T_g$ . A melt SOC was used for the calculation of birefringence above  $T_g$ , and a glassy SOC was used for the calculation of birefringence below  $T_g$ . The birefringence at  $T_g$  was stored as the contribution of the cooling induced molecular orientation and the subsequent birefringence was added to the stored values as the contribution of the residual thermal stress. The comparison of the predicted birefringence of the quenched samples with the experimental data showed that the separation of the contribution of the transient thermal stress and the residual thermal stress was successful. But the viscous-elastic material model neglected the effect of the glass transition and the stress relaxation, which might lead to numerical errors.

In this study, the flow and thermally induced birefringence of injection-compression molded discs is calculated by an integral stress-optical constitutive model with a time and temperature dependent SOC. This way, the effect of transient thermal stress and pressure on the residual birefringence is considered in the computation. The simulation results of the in-plane birefringence for compact-disc-recordable (CD-R) moldings are compared with experimental observations at different mold and melt temperatures.

## FLOW INDUCED BIREFRINGENCE

### Constitutive Models of Flow Induced Stress

A non-isothermal compressible viscous flow model has been successfully applied to simulate the flow in the injection-compression molding (19). A nonlinear viscoelastic constitutive equation is adopted for the modeling of the flow induced stress. The model was first proposed by Wagner (20, 21) as a simplified K-BKZ model (22, 23) by neglecting the Cauchy strain term in the original K-BKZ model:

$$\boldsymbol{\sigma} = -p(\rho, T)\mathbf{I} + \int_{-\infty}^t M(\xi(t) - \xi(\tau))h(I_1, I_2)\mathbf{C}_t^{-1}(\tau)d\tau \quad (1)$$

This constitutive equation is solved by a finite difference method in the time domain. Detailed algorithms can be found in Ref. (24).

In Eq 1,  $M(\xi(t) - \xi(\tau))$  is the memory function defined as follows:

$$M(\xi(t) - \xi(\tau)) = -\frac{dG(\xi(t) - \xi(\tau))}{dt} = \sum_{i=1}^m \frac{g_i}{a_T \theta_i} e^{-\frac{\xi(t) - \xi(\tau)}{\theta_i}} \quad (2)$$

where  $G(\xi(t) - \xi(\tau)) = \sum_{i=1}^m g_i e^{-\frac{\xi(t) - \xi(\tau)}{\theta_i}}$  is the shear relaxation modulus, expressed by a

discrete relaxation spectrum of  $m$  pairs of relaxation moduli  $g_i$  and relaxation times  $\theta_i$  determined by dynamic mechanical measurement;  $\xi(t)$  is the pseudo time defined by

$\xi(\tau) = \int_0^\tau \frac{1}{a_T(T)} ds$ , where  $a_T$  is the time-temperature shift factor;  $h(I_1, I_2)$  is the damping

function; and  $\mathbf{C}_t^{-1}(\tau)$  is the Finger strain tensor;  $I_1$ ,  $I_2$ , and  $I_3$  are the first, second, and

third invariants of the Finger strain tensor. The damping function proposed by Wagner et al (25) is adopted in the current study:

$$h(I_1, I_2) = m^* \exp(-n_1 \sqrt{I-3}) + (1 - m^*) \exp(-n_2 \sqrt{I-3}) \quad (3)$$

where  $m^*$ ,  $n_1$ ,  $n_2$  are material dependent constants.

The time-temperature shift factor is modeled by the WLF function (26):

$$\log(a_T) = \frac{-C_1(T - T_{ref})}{C_2 + (T - T_{ref})} \quad (4)$$

where  $C_1$ ,  $C_2$  are material dependent coefficients, and  $T_{ref}$  is a reference temperature.

The discrete relaxation spectrum is characterized by small amplitude oscillatory shear experiments. The measured storage modulus  $G'$  and the loss modulus  $G''$  between 180°C and 280°C, and their master curves for PC melt obtained by shifting the test data to a reference temperature of 180°C are shown in *Fig. 1*. The fitted coefficients of  $g_i$  and  $\theta_i$  are listed in *Table 1*. The corresponding experimental data and the fitted curve of the shift factor are shown in *Fig. 2*. The coefficients of the WLF equation are:  $C_1 = 5.09$ , and  $C_2 = 77.75^\circ\text{C}$ .

For the damping function, Laun (27) used the steady shear viscosity data and shear stress relaxation experiments to obtain the coefficients. In the current study, the damping function coefficients are obtained by fitting the complex viscosity obtained from dynamic mechanical tests. With the components substituted into *Eq 1*, the viscosity is obtained by the relationship  $\eta = \tau / \dot{\gamma}$  as:

$$\eta = \sum_{i=1}^m \left[ m^* \frac{\eta_i \theta_i^2}{(1 + n_1 \theta_i \dot{\gamma})^2} + (1 - m^*) \frac{\eta_i \theta_i^2}{(1 + n_2 \theta_i \dot{\gamma})^2} \right] \quad (5)$$

The empirical Cox-Merz rule (28) applies here, which states that the complex viscosity  $\eta^*$  is equivalent to the steady state viscosity  $\eta$  with frequency  $\omega$  replacing shear rate  $\dot{\gamma}$ . By fitting the complex viscosity according to Eq 5, the coefficients of the damping function,  $m^*$ ,  $n_1$ , and  $n_2$ , and the coefficients of the shear relaxation modulus,  $g_i$  and  $\theta_i$ , are obtained simultaneously. The complex viscosity test data and fitted curve are shown in Fig. 3 with the coefficients of the damping function being:  $m^* = 6.76\text{E-}3$ ,  $n_1 = 8.72\text{E-}14$ , and  $n_2 = 2.61\text{E-}1$ . The obtained  $g_i$  and  $\theta_i$  from the curving fitting of complex viscosity are the same as those listed in Table 1. The fitted value of the coefficient  $n_1$  is practically zero, degrading the first term of Eq 3 to a constant. Nonetheless, it is observed that the forms of the constitutive models and resulting model coefficients agree very well with the experimental data.

### Constitutive Models of Flow Induced Birefringence

A modified stress-optical rule (29) is applied to calculate the birefringence once the flow induced stress and normal stress differences are obtained from the Wagner model. In the modified stress-optical rule, instead of a linear relationship between the birefringence and the applied stress difference,

$$\Delta n = C \Delta \sigma \quad (6)$$

an integral stress-optical constitutive equation is employed to model the vertical and in-plane birefringence as follows:

$$\Delta n = \int_{-\infty}^t C(\xi(t) - \xi(\tau)) \frac{\partial \Delta \sigma}{\partial \tau} d\tau \quad (7)$$

where  $\Delta n$  is the birefringence,  $C(\xi(t) - \xi(\tau))$  is a time and temperature dependent coefficient characterized by dynamic stress-optical measurement,  $\xi(t)$  is the pseudo time as defined before,  $\Delta \sigma$  is the stress difference, and  $\tau$  is the time.

Wimberger-Friedl and Bruin (29) and Shyu et al. (30) investigated the mechanical and stress-optical behavior of PC during the transition from the glassy to the rubber state. Despite a slight scatter of data, a master curve could be constructed by shifting the test data at different temperatures, indicating that the time-temperature superposition holds for the stress-optical measurements. The time-temperature superposition of the SOC is also verified in our study as shown by the master curve in *Fig. 4* (obtained by shifting the test data from 140-175°C to a reference temperature of 220°C). The WLF coefficients for the time-temperature shift factor of the SOC are as follows:  $T_{\text{ref}}=220^\circ\text{C}$ ,  $C_1=3.03$ ,  $C_2=104.99^\circ\text{C}$ .

A KWW function introduced by Williams and Watts (31) was used by Wimberger-Friedl (29) to model the SOC. However, difficulty may arise when integration of *Eq 7* is performed with the KWW function. The similarity of *Eq 7* to the form of linear viscoelasticity inspired us that we might model the time-temperature sensitive SOC in a way analogous to shear relaxation modulus. We express the SOC with a discrete spectrum  $C_i$  and  $\lambda_i$  in the following form:

$$C(\xi(t) - \xi(\tau)) = C_0 - \sum_{i=1}^m C_i e^{-\frac{\xi(t) - \xi(\tau)}{\lambda_i}} \quad (8)$$

where  $C_i$  and  $\lambda_i$  is a spectrum of  $m$  pairs of relaxation SOCs and relaxation times. The test data of the SOC and the fitted curve are shown in *Fig. 4*, with the model parameters listed in *Table 2*.

In analogy to linear viscoelasticity, *Eq 7* is solved with a finite difference method in the time domain as follows:

$$\Delta n_{n+1} = C_0 (\Delta \sigma_{n+1} - \Delta \sigma_0) - \sum_{i=1}^m \Delta \bar{n}_{i,n+1} \quad (9)$$

where the subscript  $n+1$  denotes the values at time step  $t_{n+1}$ ,  $\Delta \sigma_0$  and  $\Delta \sigma_{n+1}$  are the current stress difference at  $t = t_{n+1}$  and initial stress difference at  $t = 0$ , and  $\Delta \bar{n}$  is a partial birefringence updated according to the following equation:

$$\Delta \bar{n}_{i,n+1} = e^{-\frac{\Delta \xi_{n+1}}{\lambda_i}} \Delta \bar{n}_{i,n} + \frac{C_i}{\Delta \xi_{n+1} / \lambda_i} (1 - e^{-\frac{\Delta \xi_{n+1}}{\lambda_i}}) \delta \Delta \sigma_{n+1} \quad (10)$$

with the subscript  $n$  indicating the value at time step  $t_n$ , and  $\delta \Delta \sigma_{n+1}$  being the increment of the stress difference within the time step  $[t_n, t_{n+1}]$ . In the above algorithm, only the values at time step  $t_n$  are stored, provided the stress history is known to the time step  $t_{n+1}$ .

The birefringence is calculated with the stress difference as follows: for vertical flow birefringence  $\Delta n_{rz}$ ,

$$\Delta \sigma = \sqrt{N_1^2 + 4\tau_{rz}^2} \quad (11)$$

and for in-plane flow birefringence  $\Delta n_{r\theta}$ ,

$$\Delta\sigma = N_2 \quad (12)$$

## THERMALLY INDUCED BIREFRINGENCE

### Constitutive Models of Thermally Induced Stress

The thermal stress calculation follows the methodology originated by Baaijens (32) with a linear viscoelastic constitutive model, where the thermal stress tensor is expressed with a hydrostatic pressure term  $p^h$  and a deviatoric stress term  $\sigma^d$ :

$$\sigma = -p^h \mathbf{I} + \sigma^d \quad (13)$$

$$p^h = -\frac{1}{3} \text{tr}(\sigma) = \int_0^t \left( \frac{\alpha}{\kappa} \dot{T} - \frac{1}{\kappa} \text{tr}(\dot{\epsilon}) \right) d\tau \quad (14)$$

$$\sigma^d = \sum_{i=1}^m 2 \int_0^t g_i e^{-(\xi(t)-\xi(\tau))/\theta_i} \dot{\epsilon}^d d\tau \quad (15)$$

Detailed derivations of *Eqs 13-15* and the algorithms to solve the equations before demolding can be found in Ref. (24). A structural finite element analysis (FEA) code was developed with axisymmetric plate elements to model the free quench after demolding (33). The structural FEA outputs the thermal stress and warpage due to asymmetric cooling with differential mold temperatures.

The storage modulus  $G'$  and the loss modulus  $G''$  of PC in the glassy state are measured by dynamic mechanical tests in the temperature range of 100-150°C. The glassy state test data combined with the melt test data in the temperature range of 100°C-280°C are shifted to a reference temperature of 150°C. The original data and the master

curves are shown in *Fig. 5*. The fitted coefficients  $g_i$  and  $\theta_i$  are listed in *Table 3*. The shift factor test data is fitted with the WLF equation for temperatures above 150°C, and the following equation for temperatures below 150°C:

$$\log(a_T) = \frac{a(1 - e^{-(b(T_{ref}-T))^c})}{d + e^{-(b(T_{ref}-T))^c}} \quad (16)$$

The measured data and fitted curve of the shift factor are shown in *Fig. 6*. The coefficients for the shift factor are:  $C_1 = 8.83$ ,  $C_2 = 35.70^\circ\text{C}$ ,  $a = 1.96$ ,  $b = 0.13$ ,  $c = 0.98$ , and  $d = 0.25$ .

### Constitutive Models of Thermally Induced Birefringence

According to Wimberger-Friedl et al. (14, 15), for free and constrained quench as well as for injection molding with the initial temperature above glass transition temperature, the thermally induced vertical birefringence is not self-equilibrating as is the thermally induced stress. The authors conclude that during the polymer cooling with temperatures above the glass transition temperature  $T_g$ , the thermal stress developed when the polymer is still in the melt state relaxes but causes molecular orientation. This cooling induced molecular orientation sets as the temperature cools below  $T_g$ . Based on the above experimental observations by Wimberger-Friedl et al., the following model is employed to calculate the vertical cooling birefringence by considering both molecular orientation during the cooling process, and the residual stress difference in the glassy state:

$$\Delta n_{rz} = \int_{-\infty}^{t_g} C(\xi(t) - \xi(\tau)) \frac{d\Delta\sigma}{d\tau} d\tau + C_g(\sigma_r - \sigma_z) \quad (17)$$

where  $t_g$  is the time when the temperature polymer at that material point just falls below  $T_g$ ,  $C_g$  is the asymptotic SOC for the glassy state, and  $\sigma_r$  and  $\sigma_z$  are the residual stresses of the radial and gapwise directions in the part. The first term in the above equation accounts for the cooling induced molecular orientation frozen in the disc, and the second term accounts for the birefringence caused by the final residual thermal stress. After demolding, the disc is assumed to be in a plane stress state, i.e.,  $\sigma_z = 0$ . Therefore, Eq 17 reduces to the following form:

$$\Delta n_{rz} = n_r - n_z = \int_{-\infty}^{t_g} C(\xi(t) - \xi(\tau)) \frac{d\Delta\sigma}{d\tau} d\tau + C_g \sigma_r \quad (18)$$

In molding practice, the injection-compression molded discs are ejected after the temperature of the core of the disc has dropped below  $T_g$ . Before ejection, the thermal stress in the radial direction is identical to that in the angular direction. Consequently, the cooling induced molecular orientation only has a negligible effect on the in-plane birefringence. The thermally induced in-plane birefringence arises only from the stress asymmetry caused by the differential mold temperatures and only occurs after demolding. Therefore, the classic stress-optical rule is applied to calculate the in-plane cooling birefringence in the glassy state:

$$\Delta n_{r\theta} = C_g (\sigma_r - \sigma_\theta) \quad (19)$$

where  $\sigma_r$  and  $\sigma_\theta$  are the residual radial and hoop stresses in the part.

## RESULTS AND DISCUSSION

The simulation of injection-compression molding process, which provides temperature and pressure fields for the birefringence prediction, has previously been described (19). Related  $P$ - $v$ - $T$ , rheological, and thermal material models and coefficients can be found in Ref. (33). CD-R substrates are injection-compression molded according to the following processing conditions. The flow rate is controlled by the screw speed, which is profiled to be slow at the start of injection and increase with the disc radius to best maintain constant melt front velocity during the filling stage. A four-stage screw speed profile is listed in *Table 4*. The diameter of the screw is 28 mm. A three-step packing pressure profile is used, which gradually decreases the packing pressure in the cavity as the melt solidifies. The profile is listed in *Table 5*. Through a coining approach, a three-step clamp force profile is used to allow the mold to open (breathe) during the filling to promote flow then to close during the packing to promote pressure uniformity and feature replication. The profile is listed in *Table 6*.

### Effect of Mold Temperature

Because of axisymmetry, the principal axes in a disc usually are aligned with the  $r$ ,  $\theta$  and  $z$  directions of the disc. The variation of the refractive indices in the disc plane is called in-plane birefringence. The in-plane birefringence is directly measured as the path difference (or retardation) of the normal incident laser beam  $\Gamma_z$ , which is the integration of the in-plane birefringence over the thickness of the disc:

$$\Gamma_z = \int_{-d/2}^{d/2} (n_r - n_\theta)_z dz \quad (20)$$

The path differences as a function of radius for mold temperatures of 100°C and 114°C with a melt temperature of 300°C are shown in *Fig. 7* (a) and (b) respectively. As the mold temperature increases from 100°C to 114°C, the in-plane birefringence decreases significantly due to more stress relaxation at higher temperature. The simulation tends to underpredict the path difference at lower radial locations with a 100°C mold temperature, and toward the rim of the disc with a 114°C mold temperature. Variation between the experimental and simulated results may be attributed to various causes, such as the nonhomogeneity of the melt temperature resulting from plastication, the irregular radial distribution of the mold temperature, and/or errors associated with the numerical calculation of the cavity pressure and stress. Regardless, the overall magnitude of the simulation compares well with the experimental data.

The gapwise distributions of the flow induced in-plane birefringence at different radial locations at the end of filling and at the end of cooling with a 100°C mold temperature are shown in *Fig. 7* (c) and (e). As can be seen from *Fig. 7* (c), the birefringence decreases rapidly with increasing radius and lower flow velocity. The development of the gapwise distribution of the birefringence is determined by the combined effects of shear rate change and temperature decay. The former is caused by the shear flow during the filling stage and subsequent packing stage due to the compressibility of the material, and the latter greatly changes the shear modulus of the polymer due to the viscoelasticity. During filling, the velocity and shear rate decrease near the mold wall due to the solidification effect, narrowing down the section for the polymer flow. As a result, the velocity and shear rate increase in the core region, with the peak shear rate occurring just outside the solidified region. This shifting of the shear rate,

coupled with modulus change caused by cooling, determines the gapwise distribution of the birefringence along the radial direction of the disc.

At the end of the filling stage, a thin layer has solidified near the surface of the disc. A global maximum and a local minimum of the birefringence can be seen in that layer, whose magnitudes are determined by the normal stress difference when the material at that gapwise position just solidifies. Another local maximum appears about halfway between the surface and the midplane of the disc, which is caused by the change of the shear rate and the shifting of the maximum of the shear rate due to the narrowing of the duct caused by the solidification effect. Near the rim of the disc (such as at  $r = 56.7\text{mm}$  in *Fig. 7 (c)*), the maximum stress is at the surface when the stress is frozen in, and no significant shear rate increase or shift of the shear rate peak will happen afterwards because no melt is conveyed past the end of flow. Therefore, the global maximum of birefringence occurs at the surface, and the local minimum about halfway between the surface and the midplane as appears at the radial positions of  $r = 30.5\text{ mm}$  and  $r = 43.6\text{ mm}$  cannot be seen at  $r = 56.7\text{mm}$ . Similar experimental results can be seen with the manipulation of the injection speed (13).

At the end of the cooling stage, almost all the birefringence in the core region has relaxed, resulting in nearly zero value in the core. The global maxima of both sides at  $r = 30.5\text{mm}$  and  $r = 43.5\text{mm}$  have decreased significantly due to the relaxation effect. The birefringence values at both surfaces for all locations remain unchanged because of the slow stress relaxation after the end of filling near the mold walls. The gapwise distributions of the flow induced in-plane birefringence at different radial locations at the end of filling and at the end of cooling for a  $114^\circ\text{C}$  mold temperature are shown in *Fig. 7*

(d) and (f). With a 114°C mold temperature, the distribution of the birefringence at the end of filling is similar to that with a 100°C mold temperature, but the global maximum is lower than that at 100°C. The location of the global maximum at a 114°C mold temperature is slightly shifted toward the surface for both sides because of the smaller thickness of the solidified layers developed at higher mold temperature. Again, the global maxima of both sides have dropped dramatically for  $r = 30.5\text{mm}$  and  $r = 43.5\text{mm}$ , and the values at the surfaces for all locations are unchanged due to the slow stress relaxation.

The gapwise distributions of flow and thermally induced vertical birefringence and their combination at  $r = 30.5\text{mm}$  for mold temperatures of 100°C and 114°C with a melt temperature of 300°C are shown in *Fig. 8* (a) and (b) respectively. The gapwise distribution of the flow induced vertical birefringence has a global maximum near the surface driven by the shear flow in the filling stage, and a local maximum of very small magnitude about halfway between the midplane and the surface of the disc determined by the packing stage. The effect of the packing pressure on the local maximum was previously reported (6, 9, 13) and can be replicated in the current simulation. It can be shown that without packing, the local maximum can be eliminated. For the injection-compression molding, the packing pressure is very low, and the time for packing stage is short (0.4 s for this study), resulting in a very low value of the local maximum. This effect also verifies that the injection-compression molding process is better than injection molding in terms of reducing flow induced residual birefringence in the molded discs. Because of the cooling induced orientation of the molecules, the thermally induced birefringence is not in a self-equilibrating state with respect to positive and negative values of birefringence, which agrees with previous experimental observations (15). The

total birefringence has a global maximum at or very close to the surface depending on the values of the flow and thermally induced birefringence. It then drops sharply into a global minimum, and then rises to reach a plateau in the core region. The birefringence in the midplane is determined by the thermally induced birefringence, and is always observed in experiments for injection or injection-compression molded parts for PC or PS (7, 9, 13, 15), although for PS, the value in the midplane is much lower compared with PC. Thus, the simulation of flow induced birefringence alone (4, 7, 9) can not adequately predict the birefringence in the midplane. Compared with a 100°C mold temperature, the 114°C mold temperature results in lower flow and thermally induced birefringence as would be expected.

### **Effect of Melt Temperature**

The path difference for melt temperatures of 300 and 320°C with a mold temperature of 100°C is shown in *Fig. 9* (a) and (b). Compared with the melt temperature of 300°C, the birefringence decreases significantly as the melt temperature increases to 320°C due to the increased stress relaxation. The overall magnitude of the predicted path difference agrees with the experimental data.

The gapwise distributions of the flow induced in-plane birefringence at different radial locations at the end of filling and at the end of cooling for 320°C melt temperature are shown in *Fig. 9* (d) and (f). The curves of the gapwise distribution of the birefringence at the end of the filling for a 320°C melt temperature follow similar trends of those for a 300°C melt temperature with reduced magnitude. As expected, a global maximum appears near the surface as the frozen-in birefringence. A local maximum is observed halfway between the midplane and the surface of the disc for radial locations

away from the rim, signifying that the normal stress difference in the core is high. At the end of the cooling, the birefringence at the core region completely relaxes, and the global maximum in the solidified layers has also decreased significantly. By comparing *Fig. 9* with *Fig. 7*, it can also be observed that the effect of melt temperature is greater than the effect of mold temperature.

The gapwise distribution of flow and thermally induced vertical birefringence and their combination at  $r = 30.5\text{mm}$  for a melt temperature of  $320^\circ\text{C}$  with a mold temperature of  $300^\circ\text{C}$  is shown earlier in *Fig. 8 (c)*. The curves at a melt temperature of  $320^\circ\text{C}$  follow similar trends as those at a melt temperature of  $300^\circ\text{C}$ , while the magnitude of the total birefringence is reduced due to facilitated stress relaxation at higher temperature. The birefringence at a  $300^\circ\text{C}$  melt temperature and a  $114^\circ\text{C}$  mold temperature has nearly the same magnitude as that at a  $320^\circ\text{C}$  melt temperature and a  $100^\circ\text{C}$  mold temperature.

## CONCLUSIONS

The flow and thermally induced in-plane and vertical birefringence is predicted for the injection-compression molded discs. Viscoelastic constitutive models are employed to calculate the flow and thermally induced stresses. An integral stress-optical constitutive model with a time and temperature dependent SOC is applied to compute the molecular orientation caused by the shear flow during the filling and packing stages, as well as by the transient cooling of the polymer. The simulation shows that for the optical grade of polycarbonate considered, the thermally induced birefringence has a similar magnitude as the flow induced birefringence. The mold and melt temperatures are shown to have a

significant effect on the predicted and observed values of birefringence. The simulation results of the path difference caused by the in-plane birefringence for CD-R moldings agree well with experimental observations under different processing conditions. The agreement signifies that the computation model well captures the transient flow orientation effect. From the comparison of the simulated in-plane birefringence with the experiment observations, one can conclude that the birefringence caused by the asymmetric cooling is significant, the neglect of which will cause significant prediction errors. Since asymmetric cooling and resultant warpage in injection and injection-compression molded parts are almost always present, much attention should be paid to the influence of the warpage when performing simulation and validation of birefringence.

#### **ACKNOWLEDGEMENT**

The authors would like to acknowledge Dr. Sam Miller (GE Plastics) and Dr. Irene Dris (GE Corporate Research and Development) for providing the material data, and colleagues in the Optical Media Development Center of GE Plastics, for enabling validation of the birefringence simulation.

## REFERENCES

- (1). A. I. Isayev, *Polym. Eng. Sci.*, 23, 271 (1983).
- (2). J. L. S. Wales, *The Application of Flow Birefringence to Rheological Studies of Polymer Melt*, Delft University Press, Rotterdam, The Netherlands (1979).
- (3). H. Janeschitz-Kriegl, *Polymer Melt Rheology and Flow Birefringence*, Springer-Verlag, Berlin (1983).
- (4). W. Dietz, J. L. White, and E. S. Clark, *Polym. Eng. Sci.*, 18, 273 (1978).
- (5). J. L. White, and W. Dietz, *Polym. Eng. Sci.*, 19, 1081 (1979).
- (6). A. A. M. Flaman, *Polym. Eng. Sci.*, 33, 193 (1993).
- (7). A. A. M. Flaman, *Polym. Eng. Sci.*, 33, 202 (1993).
- (8). I. H. Kim, S. J. Park, S. T. Chung, and T. H. Kwon, *Polym. Eng. Sci.*, 39, 1930 (1999).
- (9). I. H. Kim, S. J. Park, S. T. Chung, and T. H. Kwon, *Polym. Eng. Sci.*, 39, 1943 (1999).
- (10). J. F. Rudd, and R. D. J. Andrews, *J. Appl. Phys.*, 31, 818 (1960).
- (11). J.-P. Wu, and J. L. White, *Polym. Eng. Sci.*, 31, 652 (1991).
- (12). R. Wimberger-Friedl, and R. D. H. M. Hendriks, *Polymer*, 30, 1143 (1989).
- (13). R. Wimberger-Friedl, *Polym. Eng. Sci.*, 30, 813 (1990).
- (14). R. Wimberger-Friedl, and J. G. D. Bruin, *J. Polym. Sci. Part B: Polym. Phys.*, 31, 1041 (1993).
- (15). R. Wimberger-Friedl, *J. Polym. Sci. Part B: Polym. Phys.*, 32, 595 (1994).
- (16). R. Wimberger-Friedl, *Int. Polym. Proc.*, 11, 373 (1996).

- (17). B. Friedrichs, M. Horie, and Y. Yamaguchi, *J. Mater. Process. Manuf. Sci.*, 5, 95 (1996).
- (18). R. Wimberger-Friedl, and J. G. D. Bruin, *J. Polym. Sci. Part B: Polym. Phys.*, 31, 1051 (1993).
- (19). B. Fan, D. O. Kazmer, R. P. Theriault, and A. J. Poslinski, *Polym. Eng. Sci.*, 43, 596 (2003).
- (20). M. H. Wagner, *Rheol. Acta*, 15, 136 (1976).
- (21). M. H. Wagner, *Rheol. Acta*, 16, 43 (1977).
- (22). A. Kaye, "Non-Newtonian Flow in Incompressible Fluids," College of Aeronautics, 1962.
- (23). B. Bernstein, E. A. Kearsley, and L. J. Zapas, *Trans. Soc. Rheol.*, 7, 391 (1963).
- (24). L. F. A. Douven, PhD thesis, Eindhoven University of Technology (1991).
- (25). M. H. Wagner, T. Raible, and J. Meissner, *Rheol. Acta*, 18, 427 (1979).
- (26). J. D. Ferry, *Viscoelastic Properties of Polymers*, 3rd ed., John Wiley & Sons, Inc., New York (1980).
- (27). H. M. Laun, *Rheol. Acta*, 17, 404 (1978).
- (28). W. P. Cox, and E. H. Merz, *J. Polym. Sci.*, 28, 619 (1958).
- (29). R. Wimberger-Friedl, and J. G. D. Bruin, *Rheol. Acta*, 30, 419 (1991).
- (30). G. D. Shyu, A. I. Isayev, and C. G. Li, *J. Polym. Sci. Part B: Polym. Phys.*, 39, 2252 (2001).
- (31). G. Williams, and D. C. Watts, *Trans. Faraday Soc.*, 66, 80 (1970).
- (32). F. P. T. Baaijens, *Rheol. Acta*, 30, 284 (1991).

(33). B. Fan, D. O. Kazmer, W. C. Bushko, R. P. Theriault, and A. J. Poslinski, *J. Polym. Sci. Part B: Polym. Phys.*, 41, 859 (2003).

## **LIST OF TABLES**

Table 1. Relaxation spectrum of PC melt.

Table 2. Spectrum of the stress-optical coefficient of PC.

Table 3. Relaxation spectrum of PC (both solid and melt).

Table 4. Screw speed as a function of position.

Table 5. Packing pressure as a function of time.

Table 6. Clamp force as a function of time.

*Table 1. Relaxation spectrum of PC melt*

| $g_i$ (Pa) | $\theta_i$ (s) |
|------------|----------------|
| 9.67E+05   | 1.36E-03       |
| 5.28E+05   | 9.92E-03       |
| 4.27E+05   | 4.80E-02       |
| 1.74E+05   | 2.02E-01       |
| 5.97E+04   | 4.72E-01       |
| 1.19E+04   | 2.01E+00       |

*Table 2. Spectrum of the stress-optical coefficient of PC*

| $C_i$ (Pa <sup>-1</sup> ) | $\theta_i$ (s) |
|---------------------------|----------------|
| 5.07E-09                  |                |
| 1.18E-11                  | 1.33E-09       |
| 4.09E-11                  | 4.49E-08       |
| 2.77E-09                  | 4.38E-05       |
| 1.21E-09                  | 6.61E-06       |
| 6.84E-10                  | 2.04E-05       |
| 2.52E-10                  | 6.27E-04       |

Table 3. Relaxation spectrum of PC (both solid and melt)

| $g_i$ (Pa) | $\theta_i$ (s) |
|------------|----------------|
| 1.11E+07   | 2.92E-10       |
| 9.21E+06   | 3.60E-09       |
| 1.39E+07   | 3.41E-08       |
| 2.16E+07   | 2.80E-07       |
| 5.55E+07   | 2.80E-06       |
| 1.38E+08   | 3.12E-05       |
| 3.28E+08   | 4.45E-04       |
| 2.75E+08   | 4.50E-03       |
| 3.30E+07   | 3.79E-02       |
| 1.41E+06   | 3.34E+00       |
| 7.93E+05   | 5.65E+01       |
| 4.55E+05   | 3.84E+02       |
| 2.36E+05   | 1.93E+03       |
| 4.03E+04   | 7.00E+03       |
| 7.59E+03   | 2.40E+04       |

*Table 4. Screw speed as a function of position*

---

|               |       |       |       |       |      |
|---------------|-------|-------|-------|-------|------|
| Position (mm) | 31.50 | 29.00 | 25.00 | 6.00  | 3.50 |
| Speed (mm/s)  |       | 80.0  | 100.0 | 120.0 | 80.0 |

---

*Table 5. Packing pressure as a function of time*

|                |       |       |       |
|----------------|-------|-------|-------|
| Time (s)       | 0.05  | 0.15  | 0.40  |
| Pressure (MPa) | 48.48 | 24.24 | 12.12 |

*Table 6. Clamp force as a function of time (The ramp time is the time for the clamp force to change from one value to another. The clamp force was initially set to 0)*

|                  |     |      |      |
|------------------|-----|------|------|
| Clamp Force (kN) | 267 | 196  | 133  |
| Duration (s)     | 0.8 | 1.50 | 1.00 |
| Ramp Time (s)    | 0.2 | 0.10 | 0.50 |

## LIST OF FIGURES

- Fig. 1. Dynamic storage and loss moduli at temperatures 180-280°C (a) and the corresponding master curves at a reference temperature of 180°C (b) for PC melt
- Fig. 2. Shift factor of PC melt at a reference temperature of 180°C: experiment data vs. fitted curve
- Fig. 3. Complex viscosity of PC at 180°C: experimental data vs. fitted curve
- Fig. 4. Master curve of stress-optical coefficient (SOC) for PC at a reference temperature of 220°C: experimental data vs. fitted curve
- Fig. 5. Dynamic storage and loss moduli at temperatures 100-280°C (a) and the corresponding master curves at a reference temperature of 150°C (b) for PC
- Fig. 6. Shift factor of PC at a reference temperature of 150°C: experiment data vs. fitted curve
- Fig. 7. In-plane birefringence. (a) Path difference as a function of radial location with a melt temperature of 300°C and a mold temperature of 100°C: experiment vs. simulation. (b) Same as (a) except for a mold temperature of 114°C. (c) In-plane birefringence gapwise distribution with a melt temperature of 300°C and a mold temperature of 100°C at the end of filling. (d) Same as (c) except for a mold temperature of 114 °C. (e) Same as (c) except for at the end of cooling. (f) Same as (d) except for at the end of cooling.
- Fig. 8. Gapwise distribution of vertical birefringence. (a) Mold temperature 100°C and melt temperature 300°C ( $r=30.5\text{mm}$ ). (b) Same as (a) except for a mold temperature of 114°C. (c) Same as (a) except for a melt temperature of 320°C.

Fig. 9. In-plane birefringence. (a) Path difference as a function of radial location with a mold temperature of 100°C and a melt temperature of 300°C: experiment vs. simulation. (b) Same as (a) except for a melt temperature of 320°C. (c) In-plane birefringence gapwise distribution with a mold temperature of 100°C and a melt temperature of 300°C at the end of filling. (d) Same as (c) except for a melt temperature of 320°C. (e) Same as (c) except for at the end of cooling. (f) Same as (d) except for at the end of cooling.

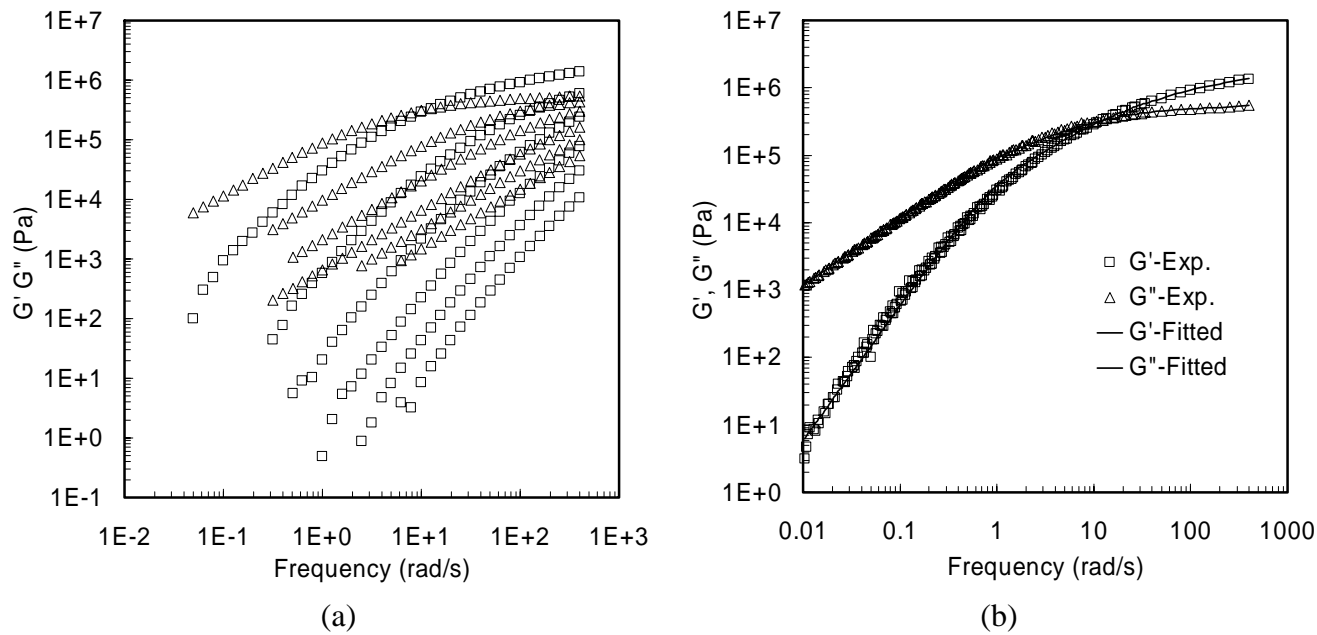
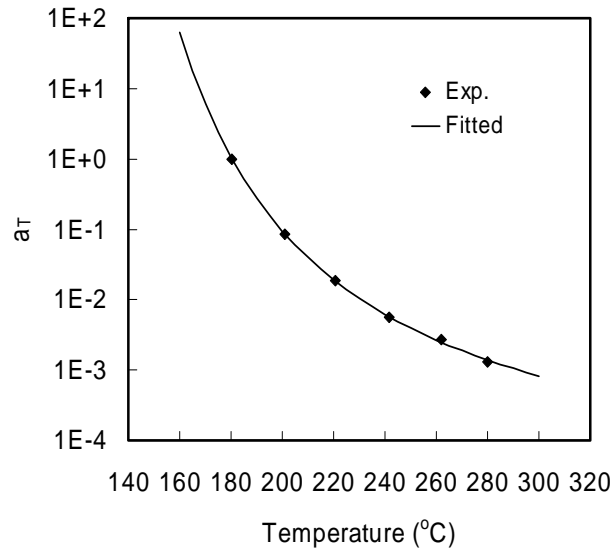
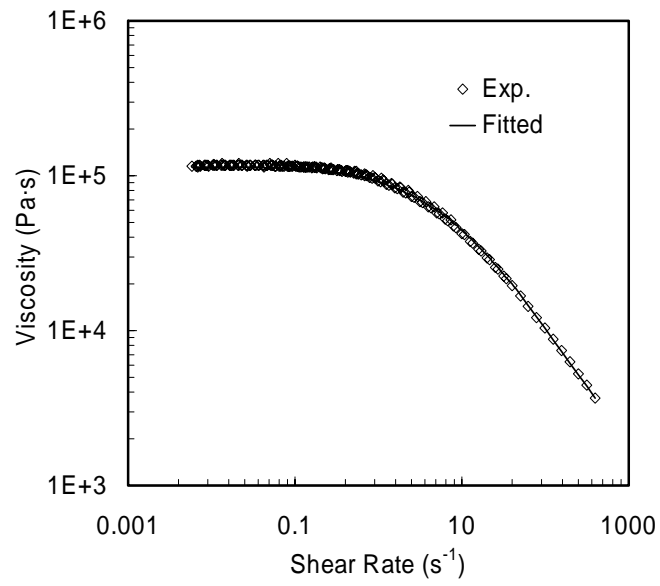


Fig. 1. Dynamic storage and loss moduli at temperatures  $180\text{-}280^\circ\text{C}$  (a) and the corresponding master curves at a reference temperature of  $180^\circ\text{C}$  (b) for PC melt



*Fig. 2. Shift facotor of PC melt at a reference temperature of 180°C: experiment data vs. fitted curve*



*Fig. 3. Complex viscosity of PC at 180°C: experimental data vs. fitted curve*

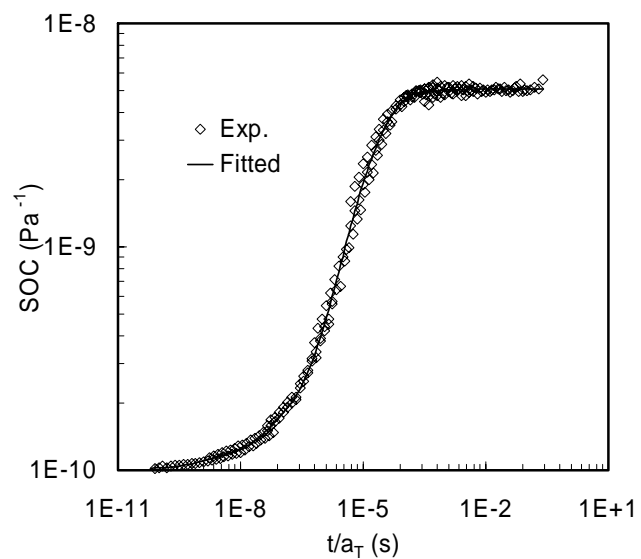


*Fig. 4. Master curve of stress-optical coefficient (SOC) for PC at a reference temperature of 220°C: experimental data vs. fitted curve*

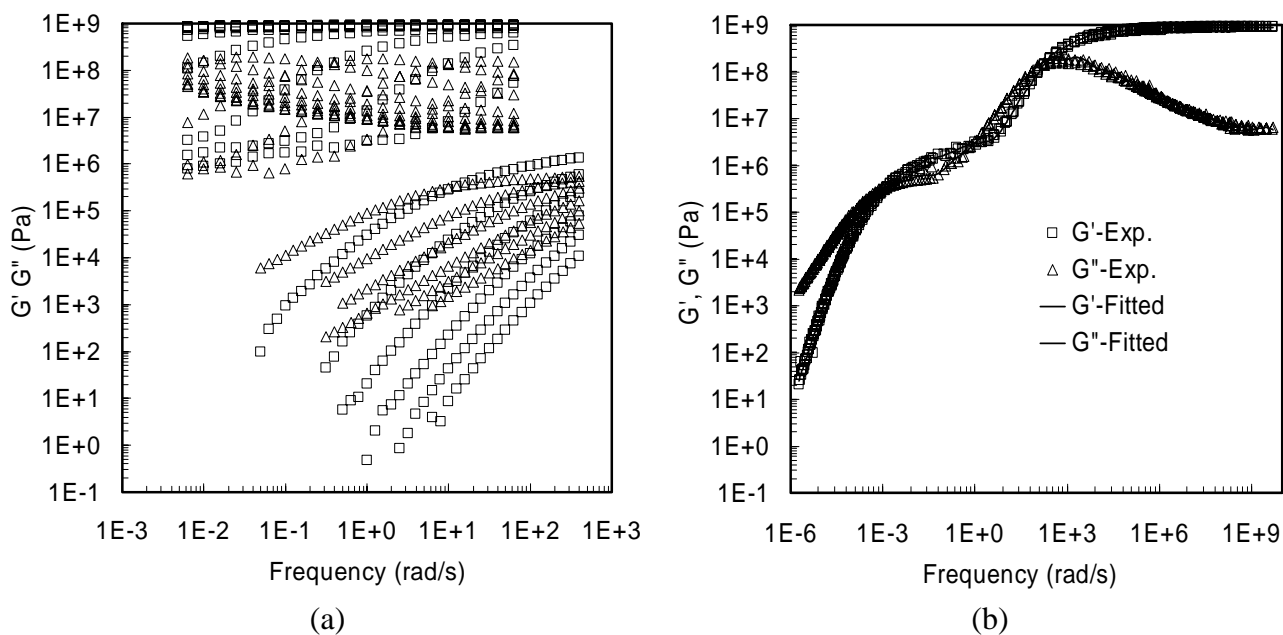
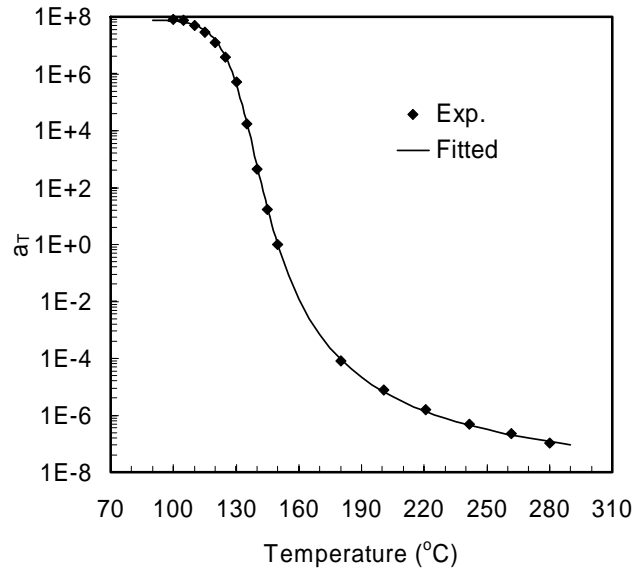
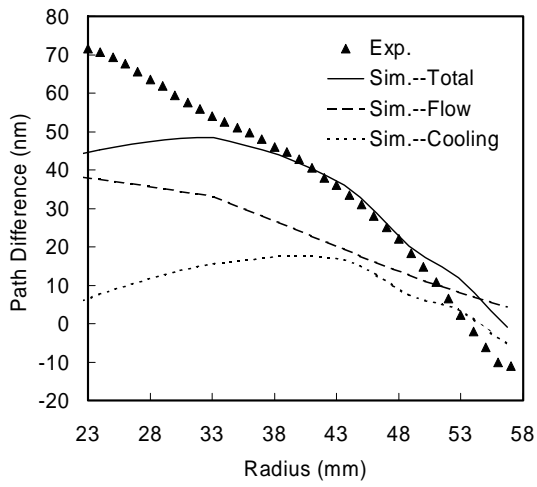


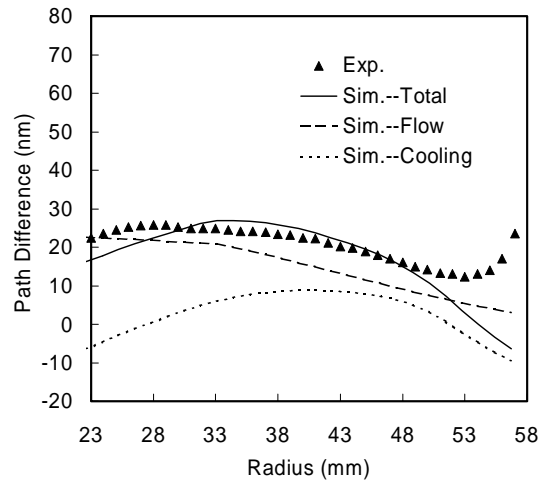
Fig. 5. Dynamic storage and loss moduli at temperatures  $100\text{-}280^{\circ}\text{C}$  (a) and the corresponding master curves at a reference temperature of  $150^{\circ}\text{C}$  (b) for PC



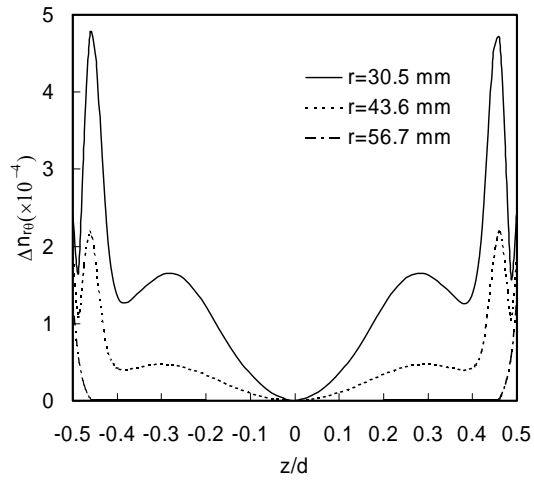
*Fig. 6. Shift facotor of PC at a reference temperature of 150°C: experiment data vs. fitted curve*



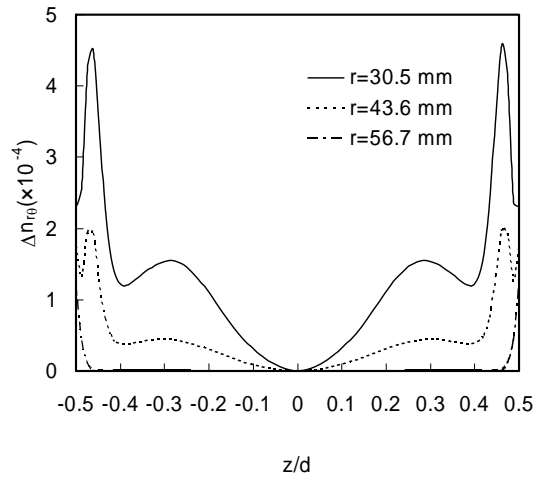
(a)



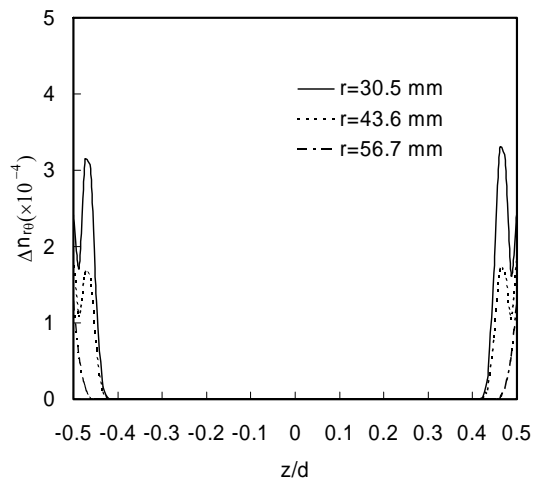
(b)



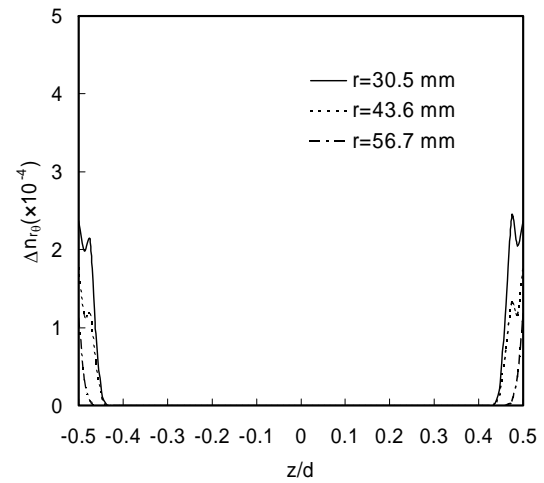
(c)



(d)

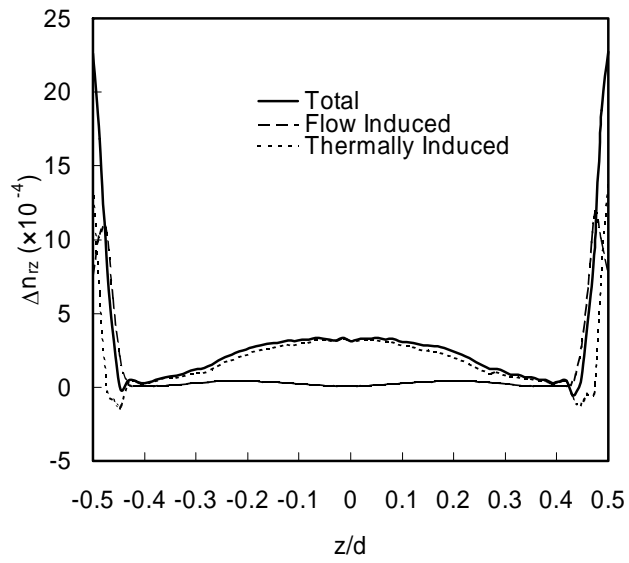


(e)

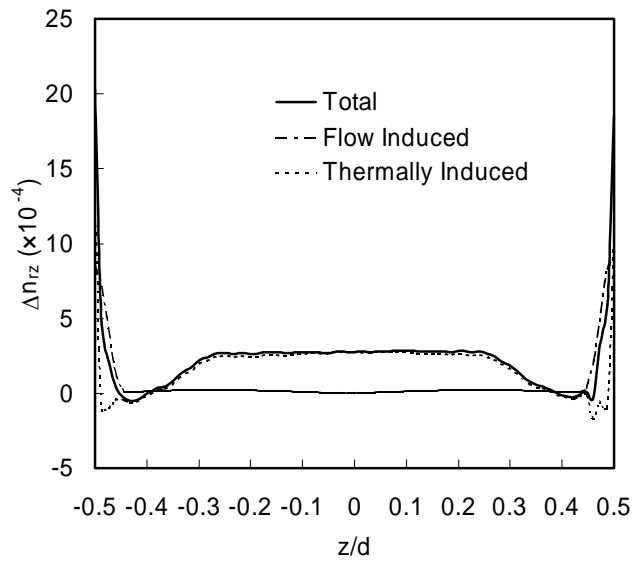


(f)

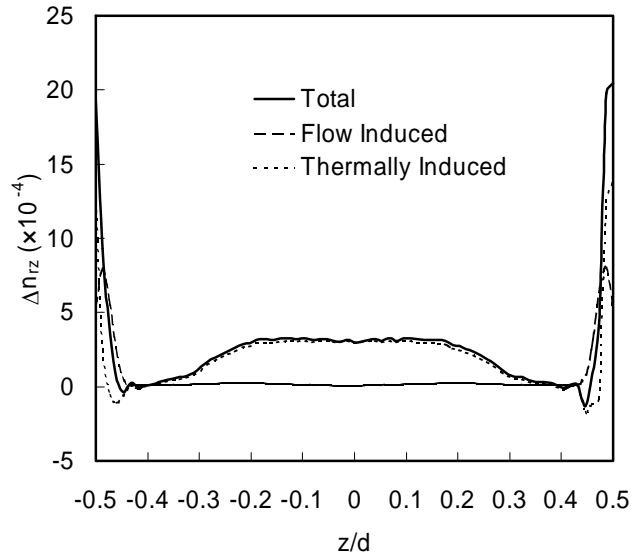
*Fig. 7. In-plane birefringence. (a) Path difference as a function of radial location with a melt temperature of 300°C and a mold temperature of 100°C: experiment vs. simulation. (b) Same as (a) except for a mold temperature of 114°C. (c) In-plane birefringence gapwise distribution with a melt temperature of 300°C and a mold temperature of 100°C at the end of filling. (d) Same as (c) except for a mold temperature of 114°C. (e) Same as (c) except for at the end of cooling. (f) Same as (d) except for at the end of cooling.*



(a)

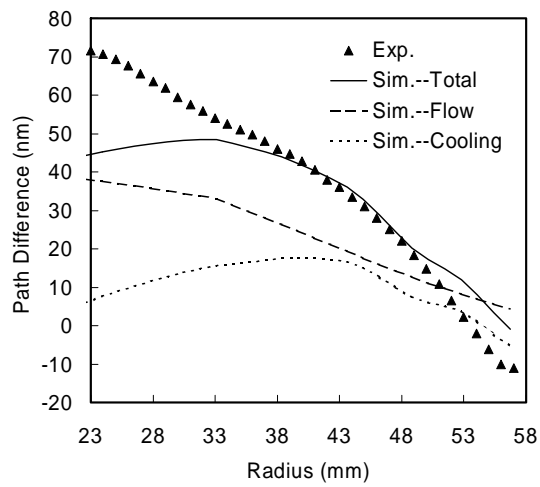


(b)

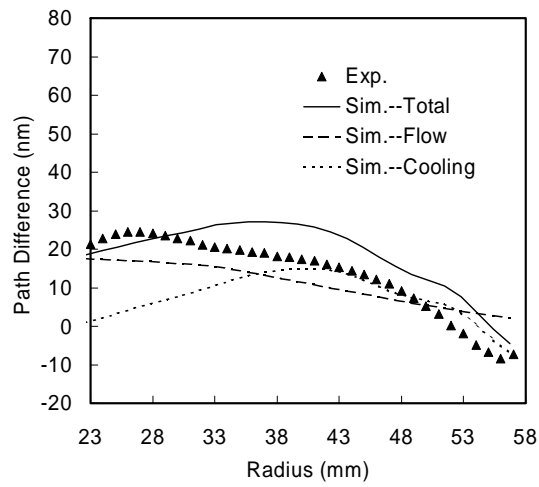


(c)

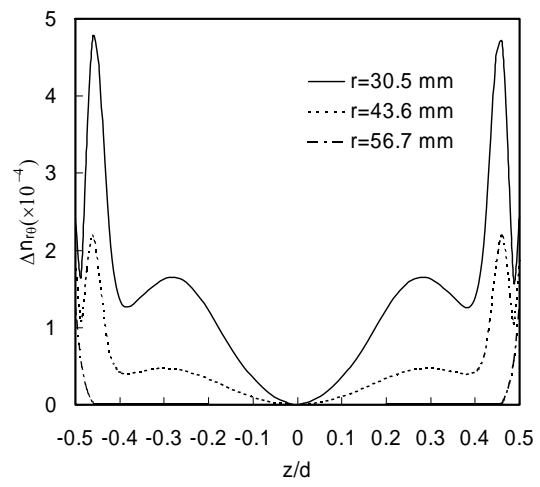
Fig. 8. Gapwise distribution of vertical birefringence. (a) Mold temperature 100°C and melt temperature 300°C ( $r=30.5\text{mm}$ ). (b) Same as (a) except for a mold temperature of 114°C. (c) Same as (a) except for a melt temperature of 320°C.



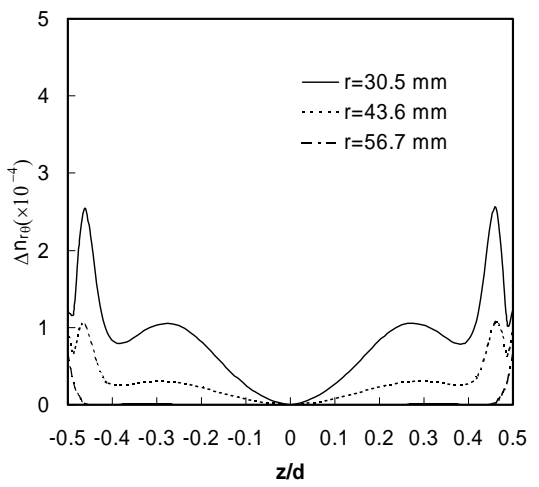
(a)



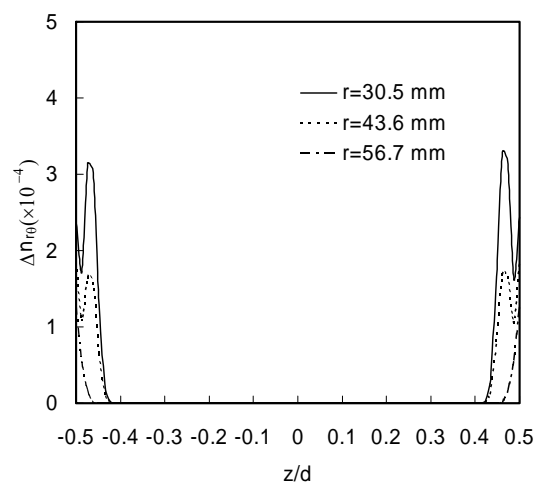
(b)



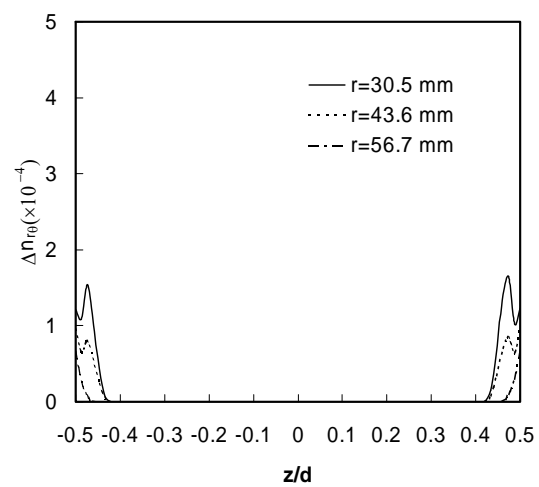
(c)



(d)



(e)



(f)

*Fig. 9. In-plane birefringence. (a) Path difference as a function of radial location with a mold temperature of 100°C and a melt temperature of 300°C: experiment vs. simulation. (b) Same as (a) except for a melt temperature of 320°C. (c) In-plane birefringence gapwise distribution with a mold temperature of 100°C and a melt temperature of 300°C at the end of filling. (d) Same as (c) except for a melt temperature of 320°C. (e) Same as (c) except for at the end of cooling. (f) Same as (d) except for at the end of cooling.*